

Inhibition of PIKfyve kinase prevents infection by EBOV and SARS-CoV-2

Yuan-Lin Kang^{1,2,3}, Yi-Ying Chou^{1,2,4}, Paul W. Rothlauf^{5,6}, Zhuoming Liu⁵, Silvia Piccinotti⁶, Timothy K. Soh⁶, David Cureton^{6,7}, James Brett Case⁸, Rita E. Chen^{5,8}, Michael S. Diamond^{5,8}, Sean P. J. Whelan^{5,*}, Tom Kirchhausen^{1,2,9,*}

¹Department of Cell Biology, Harvard Medical School, 200 Longwood Av, Boston, MA 02115, USA

²Program in Cellular and Molecular Medicine, Boston Children's Hospital, 200 Longwood Av, Boston, MA 02115, USA

³Present Address: Department of Stem Cell and Regenerative Biology, Harvard University, 7 Divinity Ave, Cambridge, MA 02138, USA

⁴Present Address: Biogen, 225 Binney Street, Cambridge, MA 02142, USA

⁵Department of Molecular Microbiology, Washington University in Saint Louis, 660 South Euclid Avenue, Saint Louis, MI 63110, USA

⁶Program in Virology, Harvard Medical School, 200 Longwood Ave, Boston, MA 02115, USA

⁷Boehringer Ingelheim Animal Health, Inc. 3239 Satellite Blvd Duluth, GA 30096, USA

⁸Departments of Medicine and Pathology & Immunology, Washington University in Saint Louis, 660 South Euclid Avenue, Saint Louis, MI 63110, USA

⁹Department of Pediatrics, Harvard Medical School, 200 Longwood Av, Boston, MA 02115, USA

* Corresponding authors:

Dr. Tom Kirchhausen

Harvard Medical School

kirchhausen@crystal.harvard.edu

phone: 617.713.8888 / fax: 617.713.8898

Dr. Sean Whelan

spjwhelan@wustl.edu

Washington University in Saint Louis

phone: 314.286.1585

36 ***Running title:* Drug inhibitors of EBOV and SARS-CoV-2 virus infection**

37

38 ***Keywords:* EBOV, SARS-CoV-2, inhibition, Apilimod, Vacuolin-1, PIKfyve,**
39 **pandemic**

40 **ABSTRACT**

41 **Virus entry is a multistep process. It initiates when the virus attaches to the host**
42 **cell and ends when the viral contents reach the cytosol. Genetically unrelated**
43 **viruses can subvert analogous subcellular mechanisms and use similar**
44 **trafficking pathways for successful entry. Antiviral strategies targeting early**
45 **steps of infection are therefore appealing, particularly when the probability for**
46 **successful interference through a common step is highest. We describe here**
47 **potent inhibitory effects on content release and infection by chimeric VSV**
48 **containing the envelope proteins of EBOV (VSV-EBOV) or SARS-CoV-2 (VSV-**
49 **SARS-CoV-2) elicited by Apilimod and Vacuolin-1, small molecule inhibitors of**
50 **the main endosomal Phosphatidylinositol-3-Phosphate/Phosphatidylinositol 5-**
51 **Kinase, PIKfyve. We also describe potent inhibition of SARS-CoV-2 strain 2019-**
52 **nCoV/USA-WA1/2020 by Apilimod. These results define new tools for studying**
53 **the intracellular trafficking of pathogens elicited by inhibition of PIKfyve kinase**
54 **and suggest the potential for targeting this kinase in developing a small-molecule**
55 **antiviral against SARS-CoV-2.**

56

57 INTRODUCTION

58 Membrane-enveloped viruses deliver their contents to cells via envelope protein-
59 catalyzed membrane fusion. Binding of virus to specific host cell receptor(s) triggers
60 membrane fusion, which can occur directly at the plasma membrane or following
61 endocytic uptake. Viruses that require endocytic uptake can use different initial
62 trafficking routes to reach the site of membrane fusion. In endosomes, acidic pH serves
63 to triggers conformational rearrangements in the viral envelope proteins that catalyze
64 membrane fusion, as seen for influenza A virus (IAV) and vesicular stomatitis virus
65 (VSV). For Ebola virus (EBOV), proteolytic processing of the envelope protein by host
66 cell proteases (Chandran et al., 2005) is necessary to expose the receptor binding
67 domain prior to engagement of Neiman Pick C1 (NPC1 or NPC Intracellular Cholesterol
68 Transporter 1) – the late endosomal-lysosomal receptor protein (Carette et al., 2011).
69 Proteolytic processing is also required for severe acute respiratory syndrome
70 coronavirus (SARS-CoV) {Wang:2008jt}, and for the current pandemic SARS-CoV-2
71 (Ou et al., 2020). Lassa fever virus (LASV) uses a different mechanism, binding alpha-
72 dystroglycan at the plasma membrane (Cao et al., 1998), for internalization with a
73 subsequent pH-regulated switch that leads to engagement of lysosomal associated
74 membrane protein 1 (LAMP1) for membrane fusion (Jae et al., 2014). Lymphocytic
75 choriomeningitis virus (LCMV) also uses alpha-dystroglycan (Cao et al., 1998) and is
76 internalized in a manner that depends on endosomal sorting complexes required for
77 transport (ESCRT) proteins (Pasqual et al., 2011), although it remains unknown
78 whether a second receptor is required.

79
80 A hallmark of the endolysosomal system is controlled dynamic trafficking of vesicular
81 carriers among its various sub-compartments. Phosphoinositides are markers for
82 defining the identity of these sub-compartments because they are restricted in their
83 distribution to specific intracellular membranes [reviewed in (Carlton and Cullen, 2005)].
84 Although it is one of the least abundant of the phosphoinositides in cells, PI(3,5)P2 is
85 particularly important for endomembrane homeostasis. It is produced by PIKfyve, which
86 phosphorylates the D-5 position in phosphatidylinositol-3-phosphate (PI3P) to yield
87 phosphatidylinositol 3,5-bisphosphate (PI(3,5)P2) (Sbrissa et al., 1999). First cloned as
88 mammalian p235 (Shisheva et al., 1999), PIKfyve is a 240 kDa class III lipid kinase,
89 present on the cytosolic face of endosomal membranes (Ikonomov et al., 2001;
90 Rutherford et al., 2006) as part of a ternary complex with SAC and ArPIKfyve (Sbrissa
91 et al., 2007).

92

93 Ablation of PIKfyve function by genetic (Ikonomov et al., 2001; 2002) or
94 pharmacological means (Cai et al., 2013; Cerny et al., 2004; Jefferies et al., 2008; Sano
95 et al., 2016; Sharma et al., 2019) causes endosomal swelling and vacuolation of late
96 endosomes and endolysosomes. It is thought that these changes result from decreased
97 membrane fission and concomitant interference in endosomal traffic (Ikonomov et al.,
98 2003; Rutherford et al., 2006).

99
100 Small-molecule inhibitors of PIKfyve, all of which have some structural resemblance to
101 each other, have been studied as potential drugs for treating cancer and autoimmune
102 diseases. These inhibitors include Apilimod (Ikonomov et al., 2011), Vacuolin-1 (Cai et
103 al., 2013), a series of 30 Vacuolin-related molecules (Cerny et al., 2004; Sano et al.,
104 2016), YM201636 (Jefferies et al., 2008), and WX8 chemical family members (Sharma
105 et al., 2019). Physiological effects of these compound in cells include inhibition of
106 autophagy (Chen et al., 2017; Lu et al., 2014; Sano et al., 2016), reduced generation of
107 IL-12/IL-23, and reduced dendritic cell infiltration in psoriasis (Wada et al., 2012).

108
109 Apilimod also inhibits infection by several viruses, including ZEBOV. Although it does
110 not alter the pH of endosomes nor inhibit cathepsin B or L (Nelson et al., 2017),
111 Apilimod blocks entry of ZEBOV and other pathogenic filoviruses (Qiu et al., 2018).
112 Several groups reported that Apilimod prevents colocalization of VSV-ZEBOV
113 pseudoviruses with the EBOV endosomal receptor NPC1, but does not prevent
114 colocalization with early endosomal antigen 1 (EEA1) (Ou et al., 2020; Qiu et al., 2018;
115 Spence et al., 2016). Apilimod also inhibits entry of pseudotyped viruses bearing the
116 spike proteins of MERS-CoV, SARS-CoV, and SARS-CoV-2, as well as of authentic
117 mouse hepatitis virus (MHV) particles (Ou et al., 2020).

118
119 Here, we have studied the effects of Apilimod on infection of VSV-eGFP-SARS-CoV-2
120 and VSV-eGFP-ZEBOV chimeras and showed that Apilimod blocks infection of both,
121 with an IC₅₀ of ~50 nM. Apilimod and Vacuolin-1 also prevented entry and infection of
122 VSV-MeGFP-ZEBOV and many of the internalized VSV-MeGFP-ZEBOV virions
123 colocalized with NCP1 in the distended, vacuolated endosomes. This suggests that
124 blocking PIKfyve kinase has the same downstream effects on these viruses, even
125 though VSV-eGFP-SARS-CoV-2 does not require interaction with NPC1 for membrane
126 fusion. Apilimod also inhibits infection by authentic SARS-CoV-2 strain 2019-
127 nCoV/USA-WA1/2020 virus, with an IC₅₀ slightly lower than its IC₅₀ for the VSV-eGFP-
128 SARS-CoV-2. We suggest that Apilimod, which has passed safety tests in previous

129 human clinical trials for non-viral indications (Burakoff et al., 2006; Krausz et al., 2012;
130 Sands et al., 2010; Wada et al., 2012), is a potential starting point for developing small-
131 molecule entry inhibitors of SARS-CoV-2 that could limit infection and disease
132 pathogenesis.

133

134 **RESULTS**

135 **Apilimod inhibits infection of VSV-MeGFP-LCVM and VSV-EBOV.** We inoculated
136 SVG-A cells with vesicular stomatitis virus (VSV) chimeras expressing the viral matrix
137 protein (M) fused to eGFP (MeGFP). The chimeras include VSV (VSV-MeGFP, which
138 initiates fusion at pH<6.2), VSV-V269H G (VSV-MeGFP-V269H, a variant of VSV G that
139 initiates fusion at pH<5.8), rabies virus G (VSV-MeGFP-RABV), Lassa virus GP (VSV-
140 MeGFP-LASV), lymphocytic choriomeningitis virus GP (VSV-MeGFP-LCMV) or Zaire
141 Ebola virus GP (VSV-MeGFP-ZEBOV). Following the incubation protocol summarized
142 in **Fig 1A**, we tested the effects on infection of Apilimod or Vacuolin-1; both compounds
143 are small-molecule inhibitors of PIKfyve kinase, which generates PI(5)P and PI(3,5)P₂
144 in late endosomes and lysosomes. Using a flow cytometry based-assay to monitor a
145 single round of infection determined by expression of viral MeGFP (**Fig. 1B**), we found
146 that Apilimod and Vacuolin-1 potently inhibit VSV-MeGFP-ZEBOV infection (**Fig. 1C**).
147 These results agree with results obtained by others with Apilimod (Hulseberg et al.,
148 2019; Nelson et al., 2017), in different cell types infected with MLV virus pseudotyped
149 with EBOV G or with Ebola virus itself (Dyall et al., 2018; Nelson et al., 2017; Qiu et al.,
150 2018). Apilimod was a less effective inhibitor of VSV-MeGFP-LCMV infection, and
151 Vacuolin-1 had no effect at the concentration used. In contrast, Apilimod and Vacuolin-1
152 failed to prevent infection by VSV-MeGFP, VSV-MeGFP-V269H, VSV-MeGFP-RABV,
153 or VSV-MeGFP-LASV (**Fig. 1C**). IN1 (Bago et al., 2014), an inhibitor of the
154 phosphoinositide kinase Vps34, the main endosomal generator of PI3P, also interfered
155 with VSV-MeGFP-LCMV and VSV-MEGFP-ZEBOV infection (**Fig. 1C**). All of these
156 viruses require low pH to trigger viral membrane fusion with the endosomal membranes,
157 and as expected, infection was fully blocked by Bafilomycin A1, which inhibits the
158 vacuolar type H⁺-ATPase (V-ATPase) acidification activity (**Fig. 1C**).

159
160 **Apilimod and Vacuolin-1 prevent cytoplasmic entry of VSV-MEGFP-ZEBOV.**
161 Productive infection requires delivery of the viral ribonucleoprotein core (RNP) into the
162 cytosol. In these experiments, we deemed RNP delivery, as monitored by single cell
163 fluorescence microscopy imaging (experimental protocol summarized in **Fig. 2A** and
164 **3A**), to be successful when fluorescent MeGFP encapsulated in the incoming virus
165 appeared at the nuclear margin of infected cells. The representative examples of VSV
166 infection and RNP core release shown in **Fig. 2B** were obtained in the absence or
167 presence of cycloheximide, which prevents viral protein expression. In the absence of
168 cycloheximide (*left panel*), large amounts of newly synthesized MeGFP are present
169 throughout the cell. In the presence of cycloheximide (*right panel*), we observed MeGFP

170 in virions (fluorescent spots) as well as released MeGFP concentrated at the nuclear
171 margin. We scored the effect of Apilimod, Vacuolin-1 or IN1 on RNP delivery by VSV-
172 MeGFP, VSV-MeGFP-V269H and VSV-MeGFP-ZEBOV by determining the appearance
173 of MeGFP at the nuclear margin in cycloheximide-treated cells. Consistent with the
174 infection results, Apilimod, Vacuolin-1 and IN1 prevented entry of VSV-Me-GFP-EBOV
175 but not of VSV-MeGFP or VSV-MeGFP-V296H. As expected, Bafilomycin A1 blocked
176 entry of all viruses (images in **Fig. 2C** and quantification in **Fig. 2D**).

177

178 **Intracellular trafficking of virus particles in the presence of Apilimod or Vacuolin-**
179 **1.** Internalized virus particles traffic along the endocytic pathway to reach the
180 endosomal compartment(s) from which membrane fusion and genome entry into the
181 cytosol occur. To establish the identity of the endosomal compartments, we used
182 genome-editing in SVG-A cells to replace expression of a subset of proteins enriched in
183 different endosomal compartments (the small GTPases Rab5c and Rab7a, EEA1, or
184 NPC1) with their corresponding fluorescent chimeras obtained by fusion with TagRFP,
185 mScarlet, or Halo (**Fig. 3B, 3C, 3E, 3F, 4B-E**). The lack of fluorescently tagged fillipin (a
186 cholesterol binder) in the endolysosomal compartment in the absence but not in the
187 presence of U18666A, a potent inhibitor of NPC1 (**Fig 4F**), showed that NPC1-Halo
188 remained active as a cholesterol transporter.

189

190 Using live-cell spinning disk confocal microscopy, we monitored the presence of virus
191 particles in the fluorescently tagged endosomes by colocalization with the fluorescent
192 spots from the virus-incorporated MeGFP. We monitored entry by carrying out the
193 experiments in the presence of cycloheximide, thus ensuring that any MeGFP
194 fluorescent signal at the nuclear margin originated only from MeGFP molecules carried
195 by incoming viral particles (**Fig. 3C**). All cells were maintained at 37°C throughout all
196 phases of the experiment to ensure normal and undisturbed intracellular trafficking. All
197 control experiments performed in the absence of inhibitors showed arrival of VSV-
198 MeGFP, VSV-MeGFP-V296H, or VSV-MeGFP-ZEBOV virus particles to early (Rab5c
199 and EEA1) (**Fig. 3D, 4E**) or late endosomes and lysosomes (Rab7a or NPC1) (**Fig. 3G,**
200 **4C, 4E**). MeGFP released from all viruses appeared at the nuclear margin, showing
201 effective RNP release. NPC1, the receptor for VSV-MeGFP-ZEBOV entry is required for
202 fusion from endosomes (Carette et al., 2011). The successful VSV-MeGFP-ZEBOV
203 infection observed in the absence of drug in cells expressing NPC1-Halo alone or in
204 combination with mScarlet-EEA1 indicates that NPC1-Halo is capable of facilitating
205 infection and that VSV-MeGFP-ZEBOV trafficked to NPC1-Halo-containing endosomes.

206
207 Apilimod and Vacuolin-1 treatment of the SVG-A cells led to enlargement and
208 vacuolization of their endosomes and lysosomes tagged with fluorescent EEA1, Rab5c,
209 Rab7a or NPC1 (**Fig. 3-5**), in agreement with earlier PIKfyve ablation studies (Ikonov
210 et al., 2003; Rutherford et al., 2006). VSV-MeGFP and VSV-MeGFP-V296H
211 (fluorescent dots, white) reached all tagged species of enlarged endolysosomes and
212 successfully penetrated into the cytosol, as indicated by MeGFP at the nuclear margin
213 (**Fig. 3E, 3F and 4C, 4D**). VSV-MeGFP-ZEBOV also trafficked to all tagged species of
214 enlarged endolysosomes, often reaching one of the numerous NPC1-containing
215 vacuoles enriched in EEA1 (**Fig. 5C**). VSV-MeGFP-ZEBOV in EEA1-containing
216 endosomes increased in the presence of Apilimod, as also reported for VLP EBOV (Qiu
217 et al., 2018). While able to reach NPC1-containing functional endosomes in cells treated
218 with Apilimod, VSV-MeGFP-ZEBOV failed to penetrate into the cytoplasm, as reflected
219 by absence of MeGFP in the nuclear margin (**Fig. 5B**).

220
221 **Apilimod blocks infection of VSV SARS-CoV-2.** Using a recombinant vesicular
222 stomatitis virus (VSV) expressing soluble eGFP (VSV-eGFP) where the glycoprotein (G)
223 was replaced with that of ZEBOV G (VSV-eGFP-EBOV) or SARS-CoV-2 (VSV-eGFP-
224 SARS-Cov-2). We inoculated MA104 cells with these chimera viruses and tested the
225 effects of Apilimod on infection by flow cytometry (**Fig. 6A**). We found potent inhibition
226 of VSV-eGFP-SARS-CoV-2 infection by Apilimod and confirmed that the compound
227 also inhibits VSV-eGFP-ZEBOV infection (**Fig. 6B, 6C**). The dose-response curves
228 indicated similar effects for VSV-eGFP-ZEBOV and VSV-eGFP-SARS-CoV-2 (IC50s ~
229 50 nM), in contrast to the absence of any detectable inhibition of VSV-eGFP infection,
230 used here as a negative control.

231
232 **Apilimod blocks infection of SARS-CoV-2 virus.**
233 To test the effect of Apilimod on bona fide SARS-CoV-2 infection, we exposed Vero E6
234 cells to fully infectious SARS-CoV-2 (strain 2019-nCoV/USA-WA1/2020); after 24 h
235 incubation, supernatants were harvested and tittered by focus-forming assay on a
236 separate set of Vero E6 cells (**Fig. 7A**). Apilimod strongly inhibited SARS-CoV-2
237 infection, and the dose-response curve was similar or better than those observed for
238 VSV-eGFP-ZEBOV or VSV-eGFP-SARS-CoV-2 (IC50s ~ 10 nM) (**Fig. 7B**).

239

240 **DISCUSSION**

241 Coronaviruses, filoviruses, and arenaviruses have different replication strategies and
242 unrelated surface glycoproteins that engage different receptor molecules during entry
243 (Cao et al., 1998; Carette et al., 2011; Chandran et al., 2005; Jae et al., 2014; Ou et al.,
244 2020; Pasqual et al., 2011). Coronavirus and filovirus surface glycoproteins share a
245 requirement for entry associated proteolytic processing for activation as fusogens
246 (Chandran et al., 2005) Filoviruses require passage through low pH compartments
247 where cathepsins are active,. Coronaviruses may enter directly by fusion at the plasma
248 membrane or following receptor mediated endocytosis. Cell entry of SARS-CoV and
249 SARS-CoV-2 depends on the protease TMPRSS2 in conjunction with ACE2 (Glowacka
250 et al., 2011; Hoffmann et al., 2020; Matsuyama et al., 2010; Shulla et al., 2011), and
251 when TMPRSS2 is present, the entry pathway becomes insensitive to cathepsin
252 inhibition (Glowacka et al., 2011; Hoffmann et al., 2020; Simmons et al., 2004).

253
254 The common inhibition of viruses from all three groups by Apilimod is a consequence of
255 perturbing their shared entry pathway. Moreover, it is not the cathepsin activity itself that
256 these compounds affect, judging from the outcome of the assays with Apilimod and
257 Vacuolin-1 showing they inhibit VSV chimeras bearing the surface glycoproteins of
258 ZEBOV and LCMV and to a lesser extent LASV. Apilimod also inhibits infection of cells
259 by VSV-SARS-CoV-2 as well as by authentic SARS-CoV-2; neither compound blocks
260 infection by wild-type VSV. For VSV-ZEBOV, we have shown that the virus reaches a
261 compartment enriched in NPC1, the EBOV co-receptor, and often also enriched in
262 EEA1, but that it nonetheless fails to release internal proteins into the cytosol. Apilimod
263 does not inhibit cathepsin (Nelson et al., 2017) but Apilimod (Baranov et al., 2019) and
264 Vacuolin-1 (Lu et al., 2014; Sano et al., 2016) can interfere with cathepsin maturation as
265 evidenced by an increase in pro-cathepsin in treated cells (Nelson et al., 2017); they
266 don't influence endosomal pH (Cerny et al., 2004; Nelson et al., 2012) although other
267 studies report Vacuolin-1 increases pH (Lu et al., 2014; Sano et al., 2016). Irrespective
268 of this discrepancy, both Apilimod and Vacuolin-1 inhibit PI-3P-5-kinase (PIKfyve) (Cai
269 et al., 2013; Sano et al., 2016), a three-subunit complex (Sbrissa et al., 2007) with a PI-
270 3P-binding FYVE domain (Sbrissa et al., 1999; Shisheva et al., 1999) that recognizes
271 the endosomal marker, PI-3-P. Functional ablation of this enzyme by genetic means
272 (Ikononov et al., 2001; 2002) gives rise to the same cellular phenotype as treatment
273 with either compound (Cai et al., 2013; Cerny et al., 2004; Sano et al., 2016). The
274 similar dose-response curves for Apilimod inhibition of the ZEBOV and SARS-CoV-2
275 chimeras (IC₅₀ of ~ 50 nM) and of authentic SARS-CoV-2 virus (IC₅₀ ~ 10 nM) are in

276 good agreement with the IC₅₀ of ~ 15 nM for Apilimod inhibition of PIKfyve *in vitro* (Cai
277 et al., 2013). Thus, perturbing normal endosomal trafficking by inhibiting PIKfyve activity
278 suggests it is the mechanism by which Apilimod and Vacuolin-1 block entry of such a
279 diverse set of viral pathogens.

280
281 One of the most striking consequence of PIKfyve inhibition, and hence of PI-3,5-P₂
282 restriction in endosomal membranes, is the swelling of endosomes into small, spherical
283 vacuoles - the phenomenon that gave Vacuolin-1 its name (Cerny et al., 2004). Our
284 imaging data with VSV-MeGFP-ZEBOV chimeras show that the virus particles
285 accumulating in these structures, many of which also contain the NPC1 co-receptor
286 (Carette et al., 2011; Côté et al., 2011), often appear to be relatively immobile and
287 adjacent to the endosomal limiting membrane. One possible explanation is that when a
288 virion reaches these distended endosomes, it can bind or remain bound to the limiting
289 membrane, but not fuse. Another is that virions may fuse with smaller intraluminal
290 vesicles in the endosomal lumen (Le Blanc et al., 2005), but that PI-3,5-P₂ depletion
291 prevents back fusion of these vesicles with the endosomal limiting membrane and
292 inhibits release into the cytosol of the viral genome.

293
294 Inhibition of infection by authentic SARS-CoV-2 shows that the blocked release of the
295 viral genome from a vacuolated endosome is independent of the shape, size, and
296 distribution of spike protein on the virion. The assay we used to determine effects on
297 infectivity of authentic virus measured release of virions after multiple rounds of
298 infection, rather than entry, which we monitored in the VSV-SARS-CoV-2 experiments
299 by detecting eGFP synthesis in the cytosol. Nevertheless, the IC₅₀ of Apilimod in
300 experiments with authentic virus is remarkably similar (or even better) to that obtained
301 with chimeric VSV-SARS-CoV-2.

302
303 Although cathepsin L inhibitors block SARS-CoV and SARS-CoV-2 infection in cell
304 culture (Ou et al., 2020; Simmons et al., 2005), they have less pronounced effects when
305 tested in animals. This may be because another protease, TMPRSS2 on the surface of
306 cells in relevant tissues, appears to prime SARS-CoV-2 spike proteins for efficient entry
307 (Hoffmann et al., 2020). As the effectiveness of Apilimod and Vacuolin-1 does not
308 depend on cathepsin inhibition, their capacity to block entry of several distinct families of
309 viruses is likely to be independent of the identity of the protease that primes their
310 surface glycoprotein for fusion. Phase I and phase II clinical trials have shown that
311 Apilimod is safe and well-tolerated (Burakoff et al., 2006; Krausz et al., 2012; Sands et

312 al., 2010; Wada et al., 2012). The trials were discontinued because of lack of
313 effectiveness against the autoimmune condition for which the drug was tested. We
314 suggest that one of these compounds, or a potential derivative, would be a candidate
315 broad-spectrum therapeutic for several emerging human viral pathogens, including
316 SARS-CoV-2.

317 **FIGURE LEGENDS**

318 **Figure 1. Apilimod and Vacuolin-1 inhibit VSV-MeGFP-ZEBOV infection.**

319 **(A)** Schematic of infectivity assay, where SVG-A cells were pretreated for 1 hour with 5
320 μ M Vacuolin, 5 μ M Apilimod, 5 μ M IN1, or 10 nM BAF A1 and subsequently infected
321 with VSV-MeGFP (multiplicity of infection, MOI = 2), VSV-MeGFP-V296H (MOI = 1),
322 VSV-MeGFP-RABV (MOI = 0.6), VSV-MeGFP-LASV (MOI = 0.6), VSV-MeGFP-LCVM
323 (MOI = 0.6) or VSV-MeGFP-ZEBOV (MOI = 0.6) for 1 hour in the presence of drugs.
324 The cells were then washed to remove unbound virus and incubated for the indicated
325 times in the presence of drugs. The cells were then fixed and the percentage of cells
326 expressing viral MeGFP was measured by flow cytometry.

327 **(B)** Representative flow cytometry results of an infection assay using VSV-MeGFP-
328 EBOV.

329 **(C)** Quantification of the infectivity is shown with averages from three independent
330 experiments per condition each determined as a duplicate measurement (error bars
331 show SEM). The statistical significance was determined using a one-way ANOVA and
332 Tukey *post-hoc* test (*, $P \leq 0.05$; **, $P \leq 0.01$; ***, $P \leq 0.001$).

333

334 **Figure 2. Apilimod and Vacuolin-1 inhibit VSV-MeGFP-ZEBOV.**

335 **(A)** Schematic of entry assay where SVG-A cells were infected with VSV-MeGFP (MOI
336 = 4), VSV-MeGFP-V296H (MOI = 4), or VSV-MeGFP-ZEBOV (MOI = 4). Experiments
337 were performed in the presence of 5 μ g/mL cycloheximide (CHX) to prevent protein
338 synthesis. Entry assay was based on the appearance of MeGFP fluorescence on the
339 nuclear margin on a per cell basis, of fixed infected cells visualized by fluorescence
340 microscopy. Staining the fixed cells with Alexa647 labeled wheat germ agglutinin
341 identified the plasma membrane of each cell (dashed outlines in **C**).

342 **(B)** Virus infection in the absence of CHX (left panel) resulted in the appearance of
343 MeGFP fluorescence throughout the cell volume. The presence of CHX resulted in virus
344 entry being observed by MeGFP fluorescence at the nuclear margin, which was
345 released from incoming viral particles (right panel, white arrows). Scale bar indicates 10
346 μ m.

347 **(C)** Representative examples of maximum-Z projection images from the whole cell
348 volume obtained with optical sections separated by 0.3 μ m using spinning disc confocal
349 microscopy. Scale bar indicates 10 μ m.

350 **(D)** Quantification of the number of cells with nuclear margin labeling from three
351 independent experiments each determined from fields containing 59-90 cells (error bars

352 show SEM). The statistical significance of the entry data was analyzed for statistical
353 significance by one-way ANOVA and Tukey post-hoc test (***, $P \leq 0.001$).

354

355 **Figure 3. Endolysosomal traffic of VSV-MeGFP-ZEBOV in cells expressing**
356 **TagRFP-Rab5c or TagRFP-Rab7a in the presence of Apilimod or Vacuolin-1.**
357 **(Associated Videos 1 and 2).**

358 **(A)** Schematic of live cell imaging experiment using SVG-A cells expressing
359 fluorescently tagged TagRFP-Rab5c or TagRFP-Rab7a. Cells were infected with VSV-
360 MeGFP, VSV-MeGFP-V296H or VSV-MeGFP-ZEBOV (MOI = 4). Viruses trafficking
361 (monitored with MeGFP) to the endo-lysosomal system (recognized by their labeling
362 with TagRFP-Rab5c or TagRFP-Rab7a) and virus entry (established by MeGFP at the
363 nuclear margin) were ascertained by live-cell fluorescence imaging using a spinning disc
364 confocal microscope.

365 **(B)** Visualization of VSV-MeGFP infection in TagRFP-Rab5c cells in the absence (left
366 panel) or presence of CHX (right panel, white arrows) using live-cell imaging. Scale bar
367 represents 10 μm .

368 **(C)** Genomic PCR analysis of SVG-A cells showing biallelic integration of TagRFP into
369 the *RAB5C* genomic locus by cotransfection of a plasmid coding for Cas9, a linear PCR
370 product coding for the specific gRNAs targeting a region near the ATG codon of Rab5c
371 under the control of the U6 promoter, and a template plasmid containing the RFP
372 sequence flanked by 800 base pairs upstream and downstream of the targeted region
373 (see materials and methods for more details) to generate a clonal gene-edited cell-line
374 expressing TagRFP-Rab5c.

375 **(D)** Representative examples of maximum-Z projection images from four optical
376 sections spaced 0.35 μm apart of virus entry in the absence of drug, or in the presence
377 of IN1, Vacuolin, or Apilimod (from left to right) for VSV (top), VSV-V269 (middle), and
378 VSV EBOV (bottom). Each condition is in the presence of CHX. All viruses reach
379 Rab5c-containing endosomes but only VSV-MeGFP-ZEBOV fails to penetrate in the
380 presence of IN1, Vacuolin-1, or Apilimod. Scale bars are 10 μm . Insets correspond to a
381 single optical section with scale bars of 3 μm .

382 **(E)** Visualization of VSV infection in TagRFP-Rab7a cells in the absence of CHX (left
383 panel) and entry in the presence of CHX (right panel, white arrows) with scale bar
384 indicating 10 μm .

385 **(F)** Genomic PCR analysis showing biallelic integration of RFP into the *RAB7A* genomic
386 locus to generate a clonal gene-edited cell-line expressing TagRFP-Rab7a, using the
387 same approach as used for Rab5C.

388 **(G)** Representative examples of maximum-Z projection images of virus entry (in the
389 presence of CHX) in the absence of drug, or in the presence of IN1, Vacuolin, or
390 Apilimod (from left to right) for VSV-MeGFP (top), VSV-MeGFP-V296H (middle), and
391 VSV-MeGFP-ZEBOV (bottom). All viruses reach Rab7a-containing endosomes but
392 only VSV-MeGFP-ZEBOV fails to penetrate in the presence of IN1, Vacuolin-1 or
393 Apilimod. Scale bars are 10 μm . Insets correspond to a single optical section with scale
394 bars of 3 μm .

395

396 **Figure 4. Endolysosomal traffic of VSV-MeGFP-ZEBOV in cells expressing NPC1-**
397 **Halo or coexpressing mScarlet-EEA1 and NPC1-Halo in the presence of Apilimod.**
398 **(Associated Video 3).**

399 **(A)** Schematic of live cell imaging experiment with gene-edited SVG-A cells expressing
400 NPC1-Halo or NPC1-Halo together with mScarlet-EEA1. Halo was labeled with either
401 JF549 or JF647. Cells were infected with VSV-MeGFP-ZEBOV (MOI = 3).

402 **(B)** Genomic PCR analysis showing biallelic integration of Halo into the *NPC1* genomic
403 locus to generate a clonal gene-edited cell-line expressing NPC1-Halo, using the same
404 approach as for Rab5C and Rab7A.

405 **(C)** Representative examples of maximum-Z projection images from four optical
406 sections spaced 0.25 μm apart in the absence (left) and presence of Apilimod (right)
407 showing that VSV-MeGFP-ZEBOV reached NPC1-Halo-containing endosomes even in
408 the presence of Apilimod, while failing to penetrate and infect. Scale bar indicates 10
409 μm . Insets correspond to a single optical section with the scale bar indicating 3 μm .

410 **(D)** SVG-A cells with genomic NPC1-Halo were further gene edited to contain EEA1
411 tagged with mScarlet. Genomic PCR analysis shows biallelic integration into the *EEA1*
412 locus of mScarlet-EEA1 (left) and into the *NPC1* locus of NPC1-Halo (right).

413 **(E)** Representative examples of maximum-Z projection images in the absence (left) and
414 presence of Apilimod (right) showing that VSV-MeGFP-ZEBOV reached endosomes
415 containing mScarlet-EEA1 and endosomes containing both mScarlet-EEA1 and NPC1-
416 Halo in the presence of Apilimod, while failing to penetrate and infect. Scale bar
417 indicates 10 μm . Insets correspond to a single optical section with scale bar indicating 3
418 μm .

419 **(F)** Representative images of parental (top) and gene-edited SVG-A cells expressing
420 NPC1-Halo (bottom) incubated with filipin III (naturally fluorescent polyene antibiotic
421 that binds to cholesterol) in the absence (left) and presence of U18666A (right, NPC1
422 inhibitor of cholesterol export) showing NPC1-Halo is a functional cholesterol
423 transporter.

424

425 **Figure 5. Extent of VSV-MeGFP-ZEBOV traffic into endosomes enriched in**
426 **NPC1-Halo or NPC1-Halo and mScarlet-EEA1.**

427 **(A)** Schematic of imaging experiment of VSV-EBOV trafficking in NPC1-Halo or NPC1-
428 Halo and mScarlet-EEA1 gene edited SVG-A cells.

429 **(B)** Representative examples of maximum-Z projection images from four optical
430 sections spaced 0.25 μm apart in the absence and presence of Apilimod after 2 or 4
431 hours post infection.

432 **(C)** Quantification of VSV-MeGFP-EBOV colocalization with mScarlet-EEA1 alone, both
433 mScarlet-EEA1 and NPC1-Halo, or NPC1-Halo alone. At 2 hours post infection, 73 and
434 95 cells were quantified in the absence or presence of 5 μM Apilimod, respectively. At 4
435 hours, 55 and 147 cells were quantified in the absence or presence of 5 μM Apilimod,
436 respectively. Data is presented as % colocalization within the three types of labeled
437 endosomes.

438

439 **Figure 6. Apilimod and Vacuolin-1 inhibit infection of VSV-eGFP-SARS-Cov-2**

440 **(A)** Schematic of infectivity assay of VSV-eGFP, VSV-eGFP-ZEBOV, and VSV-eGFP-
441 SARS-CoV-2 in MA104 cells. MA104 cells were pretreated for 1 h with the indicated
442 concentration Apilimod. Pretreated cells were inoculated with the indicated virus (MOI =
443 1) for 1h at 37°C. At 6 hours post infection cells were harvested and the fraction of cell
444 expressing eGFP cells quantified by flow cytometry.

445 **(B)** Quantification of the infectivity is shown with averages +/- SEM from three
446 independent experiments. Statistical significance was determined using a T-test (*, $P \leq$
447 0.05; **, $P \leq 0.01$).

448

449 **Figure 7. Apilimod inhibits infection of SARS-CoV-2 virus**

450 **(A)** Schematic of infectivity assay of fully infectious Sars-CoV-2 (strain 2019-nCoV/USA-
451 WA1/2020). Vero E6 cell monolayers were pretreated with medium containing DMSO
452 or serial dilutions of Apilimod at the indicated concentrations. SARS-CoV-2 was diluted
453 (MOI = 0.01) in Apilimod-containing medium and added to Vero E6 cells for 1 h at 37°C.
454 After adsorption, the viral inocula were removed, and medium containing the respective
455 concentration of Apilimod was reapplied. After 24 h incubation, supernatants were
456 harvested and tittered by focus-forming assay on a separate set of Vero E6 cells.

457 **(B)** Quantification of the infectivity is shown with averages +/- SEM from three
458 independent experiments per condition and expressed as the percent inhibition relative
459 to mock-treated SARS-CoV-2 infected cells.

460 **Video 1. Apilimod doesn't inhibit VSV-MeGFP entry.** Maximal Z-projection from four
461 optical sections separated 0.25 um apart of SVG-A cells gene-edited to express
462 TagRaFP-Rab5c imaged by spinning disc confocal microscopy every 3 seconds for 3
463 min. Cells were infected with VSV-MeGFP (MOI = 4) in the presence of CHX with or
464 without 5 uM Apilimod and imaged ~ 3-4 hr post-infection.

465
466 **Video 2. Apilimod inhibits VSV-MeGFP-ZEBOV entry.** Maximal Z-projection from four
467 optical sections separated 0.25 um apart of SVG-A cells gene-edited to express
468 TagRFP-Rab5c imaged by spinning disc confocal microscopy every 3 seconds for 3
469 min. Cells were infected with VSV-MeGFP-ZEBOV (MOI = 3) in the presence of CHX
470 with or without 5 uM Apilimod and imaged ~ 6-7 hr post infection.

471
472 **Video 3. Apilimod inhibits VSV-MeGFP-ZEBOV entry.** Maximal Z-projection from four
473 optical sections separated 0.25 um apart of SVG-A cells gene-edited to express NPC1-
474 Halo imaged by spinning disc confocal microscopy every 3 seconds for 3 min. Cells
475 were infected with VSV-MeGFP-ZEBOV (MOI = 3) with or without 5 uM Apilimod and
476 imaged ~ 5 hr post infection.

477

478 **MATERIAL AND METHODS**

479 **Cell culture**

480 Human astroglial SVG-A derived cells (a kind gift from Walter J. Atwood) were grown at
481 37°C and 5% CO₂ in Minimum Essential Medium (MEM) (10-010-CV; Corning)
482 supplemented with 10% heat inactivated fetal bovine serum (S11150; Atlanta
483 Biologicals), penicillin and streptomycin (1406-05-9; VWR International). African Green
484 Monkey kidney epithelial MA104 cells (a kind gift from Siyuan Ding, WUSM) were grown
485 at 37°C and 5% CO₂ in Medium 199 supplemented with 10% heat inactivated fetal
486 bovine serum. Vero C1008 [Vero 76, clone E6, Vero E6] (ATCC CRL-1586) cells were
487 cultured in Dulbecco's Modified Eagle Medium (DMEM) supplemented with 10% fetal
488 bovine serum, and penicillin and streptomycin. Vero CCL-81 (ATCC CCL-81) cells were
489 maintained in DMEM supplemented with 10% FBS, 10mM HEPES pH 7.4, 1%
490 Glutamax, and penicillin/streptomycin.

491

492 **Reagents**

493 Vacuolin-1 (Cerny et al., 2004) was custom synthesized; Apilimod (HY-14644) was from
494 MedChem Express, IN1 was a kind gift from Dr. N. Gay (Bago et al., 2014), U-18666A
495 (10009085), and Fillipin III (70440) were from Cayman Chemical, Bafilomycin A1
496 (B1793-2UG) was from Sigma-Aldrich, Cycloheximide (239764) was from Calbiochem,
497 and wheat germ agglutinin conjugated with Alexa Fluor®-647 (W32466) was from
498 ThermoFisher.

499

500 **Viruses**

501 Recombinant VSV (Indiana serotype) expressing MeGFP alone which initiates fusion at
502 pH<6.2 (VSV-MeGFP) (Soh and Whelan, 2015) (or in combination with V269H G, VSV-
503 MeGFP-V296H), RABV G (VSV-MeGFP- RABV), LASV G (VSV-MeGFP-LASV) (Jae et
504 al., 2014), LCMV G (VSV-MeGFP-LCMV), Zaire EBOV G (VSV-MeGFP-ZEBOV) (Wong
505 et al., 2010) or SARS-CoV-2 S Wuhan-Hu-1 strain (VSV-eGFP-SARS-CoV-2 –
506 description to be published elsewhere) were used for infection, entry and live cell
507 imaging assays. All viruses were generated and recovered according to (Whelan et al.,
508 1995).

509

510 SARS-CoV-2 strain 2019-nCoV/USA-WA1/2020 was obtained from the Centers for
511 Disease Control and Prevention (gift of Natalie Thornburg). Virus was passaged once in
512 Vero CCL81 cells (ATCC) and titrated by focus-forming assay also on Vero E6 cells.

513

514 **Genome-editing**

515 Individual cell lines of SVG-A were gene edited in both alleles using the CRISPR/Cas9
516 system to incorporate fluorescent tags into the N-terminus of Rab5c (TagRFP), Rab7a
517 (TagRFP), EEA1 (mScarlet) or the C-terminus of NPC1 (Halo). The NPC1-Halo
518 expressing cells were further gene edited to incorporate mScarlet-EEA1 creating SVG-A
519 cells simultaneously expressing mScarlet-EEA1 and Halo-NPC1-Halo.

520

521 A free PCR strategy (Chou et al., 2016; Ran et al., 2013) was used to generate small
522 guide RNAs (sgRNA) with target sequences for either Rab5c, Rab7a, NPC1, or EEA1.

523

524 The genomic DNA fragment of Rab5c, Rab7a, NPC1, or EEA1 genes fused with either
525 RFP, Halo, or mScarlet were cloned into the pUC19 vector (donor constructs) which
526 then served as homologous recombination repair templates for the Cas9 enzyme-
527 cleaved genomic DNA. Donor constructs were obtained by a ligation of PCR
528 amplification products from the genomic DNA fragments, TagRFP, Halo, and mScarlet
529 sequences. Primers F1-R1 and F3-R3 amplified approximately 800 base pairs of
530 genomic sequences upstream and downstream of the start codon of Rab5c, Rab7a or
531 EEA1, or the stop codon of NPC1, respectively. Primers F1 and R3 contain sequences
532 complementary to the pUC19 vector linearized using the SmaI restriction enzyme (lower
533 case in the primer sequences). The TagRFP sequence containing the GGS peptide
534 linker was amplified using primers F2-R2 from a TagRFP mammalian expression
535 plasmid used as a template. The F2 primer contains complementary sequences to the
536 3' end of the F1-R1 fragment, while the F3 primer contains complementary sequences
537 to the 3' end of the TagRFP sequences. PCR products (fragments F1-R1, F2-R2, and
538 F3-R3) were subjected to electrophoresis in 1% agarose and gel purified using a
539 purification kit from Zymogen. The PCR fragments were cloned into the linearized
540 pUC19 vector using the Gibson Assembly Cloning Kit (E5510S; New England Biolabs).

541

542 Primer sequences used to generate the sgRNAs and corresponding genomic
543 fragments:

Primer Description		Sequence
U6 promoter	forward primer	5' GCCGTACCTGAGGGCCTATTTCCC 3'
	reverse primer	5'ACCTCTAGAAAAAAGCACCGACTCGGTGCCACTTTTTCAAGTTGATAACGGACTAGCCTATTTTAACTGTCTATTCTAGCTCTAAAAACNNNNNNNNNNNNNNNNNNNNNNCGGTGTTTCGTCTTTCCACAAG 3
target sequence for reverse primer	rab5c	GACCCGCCATTGCCGTCCA
	rab7a	TCAAATAAAGGGGAAAAG
	NPC1	TAAATTTCTAGCCCTCTCGC
	EEA1	GGTGGTGGTTAAACCATG
Rab5c	F1	gaattcgagctcggtagccGAGAGAACTAGGGAAGAAGGATCAG
	R1	TGCCCGTCCAGCTGTAGTG
	F2	CCACTACAGCTGGACGGCAatggtgtctaaggcgaagagc
	R2	GGAACCACCAGAACCACCAGAA
	F3	GGTTCTGGTGGTTCTGGTGGTTCCCTGGCGGTCGGGGAGGCGCA
	R3	gtcgactctagaggatccccCCTCTACCAAGAGAGTAGAGAAAG
Rab7a	F1	gaattcgagctcggtagccACTGTGTGACGCTTGCCTTCA
	R1	CCTTCAAATAAAGGGGAAAAGG
	F2	CCTTTTCCCCCTTAGTTTGAAGGatggtgtctaaggcgaag
	R2	GGAACCACCAGAACCACCAGAA
	F3	TTCTGGTGGTTCTGGTGGTTCCACTCTAGGAAGAAAGTGTGCTG
	R3	gtcgactctagaggatccccCCTCAACCACTACACAGAAT
NPC1	F1	gaattcgagctcggtagccCCTACTGAGATGAAGGAGTCCAT
	R1	GAAATTTAGAAGCCGTTTCGCGC
	F2	CGCGAACGGCTTCTAAATTTGgaggttctggtgttctggtgttccGAGAAATCGGTACTGGCTTTCCA
	R2	GCCGAAATCTCGAGCGTCGACAG
	F3	CTGTGACGCTCGAGATTTCCGGCtagccctctcagggcatcc
	R3	gtcgactctagaggatccccGCTGTCTAATGAAACTTCTAGTTC
EEA1	F1	gaattcgagctcggtagccCTCTTTGGCTGAAATAGAAGCAGG
	R1	CATGGTTTAAACCACCCGCGG
	F2	CGCCGGTGGTGGTTAAACCATGgtgagcaagggcgagcgagtgat
	R2	ctgtacagctcgtccatccgc
	F3	GCGGCATGGACGAGCTGTACAAGgaggttctggtgttctggtgttccTAAAGGAGGATTTACAGAGGGTAAGAG
	R3	gtcgactctagaggatccccGCTCTAATCTTCTATCTCAAGGTTTTTC

544

545 SVG-A cells (1.5×10^5 cells) were co-transfected with 0.8 μg of *Streptococcus*
 546 *pyogenes* Cas9, 0.8 μg free PCR product coding for the target sgRNA, and 0.8 μg
 547 pUC19 vector using Lipofectamine 2000 reagent (Invitrogen) according to the
 548 manufacturer's instructions. Transfected cells were grown for 7 to 10 days and sorted
 549 for TagRFP, Halo, or mScarlet expression using fluorescence-activated cell sorting
 550 (FACS) (SH-800S; Sony). Prior to FACS, NPC1-Halo cells were labeled for 15 minutes
 551 with Janelia FluorTM 647 (JF647). Single cells expressing the desired chimera were
 552 isolated, clonally expanded, and then screened by genomic PCR for TagRFP, Halo, or
 553 mScarlet insertion into both alleles.

554

555 Primer sequences used for screening:

Primer Description		Sequence
Rab5C	typing forward	GAGCCTGAAGTTGGGAGACC
	typing reverse	CATGCCCACTCACCTCCAAT
Rab7a	typing forward	GCGGTCACCTCTTTGAGAAAGT
	typing reverse	AAGTGGCAGCACGGACAGTGT
NPC1	typing forward	TCTCCAAAAGAGAGGGAGAGAGAT
	typing reverse	AAGTTTAGTGTCTGTGTTGCCT
EEA1	typing forward	CATCTGTCAGTTACGGGGGCTG
	typing reverse	CGGCACCACACCCTCCAGCTC

556

557 **Infection assays**

558 SVG-A cells were plated at about 30-40 % confluency into 24-well plates and incubated
559 for 1 day at 37°C and 5% CO₂. At the start of the experiment, cells were incubated with
560 the indicated drug or DMSO at 37°C for one hour. Following this, cells were incubated
561 for one hr at 37°C with VSV, VSV-MeGFP-V296H, VSV-MeGFP-RABV, VSV-MeGFP-
562 LASV, VSV-MeGFP-LCVM or VSV-MeGFP-ZEBOV in drug or DMSO-containing
563 infection medium (α -MEM, 50mM HEPES, 2% FBS). Cells were then washed to remove
564 non-adsorbed viruses and further incubated at 37°C in medium containing the drug or
565 DMSO with experiments ending at the indicated times by fixation with 3.7%
566 formaldehyde in PBS. Fluorescent intensity from 20,000 single cells from a single round
567 of infection was determined by flow cytometry using a BD FACSCanto™ II equipped
568 with DIVA software package.

569
570 MA104 cells were pretreated for one h with the indicated concentration Apilimod or
571 DMSO. Pretreated cells were inoculated with VSV-eGFP, VSV-eGFP-EBOV or VSV-
572 eGFP-SARS-Cov-2 at an MOI = 1 (based on titers in MA104 cells) in the presence of
573 Apilimod or DMSO for one hour at 37°C. Six to 8 hour post infection, cells were
574 collected and fixed in 2% PFA and then subjected to flow cytometry. The percentage of
575 GFP cells was determined using FlowJo software (Tree Star Industries, Ashland, OR).

576
577 Vero E6 cell monolayers were pretreated for 1 h at 37°C with serial dilutions of Apilimod
578 at the indicated concentrations. Next, SARS-CoV-2 was diluted to an MOI of 0.01 focus-
579 forming units (FFU)/cell in Apilimod-containing medium and added to Vero E6 cells for 1
580 h at 37°C. After adsorption, cells were washed once with PBS, and medium containing
581 the respective concentration of Apilimod was added. Cell were incubated for a 24 h at
582 37°C, and at which time cell culture supernatants were removed and used for
583 determination of viral titer by focus forming assay.

584
585 **SARS-CoV-2 focus forming assay**

586 Cell culture supernatants from virus-infected cells were diluted serially 10-fold and
587 added to Vero E6 cell monolayers in 96-well plates and incubated at 37°C for 1 h.
588 Subsequently, cells were overlaid with 1% (w/v) methylcellulose in MEM supplemented
589 with 2% FBS. Plates were harvested 30 h later by removing overlays and fixed with 4%
590 paraformaldehyde in PBS for 20 min at room temperature. Plates were washed and
591 sequentially incubated with 1 μ g/mL of CR3022 anti-spike antibody (Yuan et al., 2020)
592 and HRP-conjugated goat anti-human IgG in PBS supplemented with 0.1% saponin and

593 0.1% BSA. SARS-CoV-2-infected cell foci were visualized using TrueBlue peroxidase
594 substrate (KPL) and quantitated on an ImmunoSpot microanalyzer (Cellular
595 Technologies). Data were processed using Prism software (GraphPad Prism 8.0) and
596 viral titers are reported as percent inhibition relative to mock-treated SARS-CoV-2
597 infected cells.

598

599 **Entry assay and intracellular traffic**

600 SVG-A cells plated on glass #1.5 coverslips at about 30-40 % confluency one day prior
601 to experiment were treated with drug or DMSO for one hr at 37°C. Following this, cells
602 were incubated at 37°C with VSV, VSV-MeGFP-V296H, VSV-MeGFP-RABV, VSV-
603 MeGFP-LASV, VSV-MeGFP-LCVM or VSV-EBOV (also expressing MeGFP) in drug or
604 DMSO containing infection medium. After this, cells were washed then further incubated
605 in medium containing the drug or DMSO at 37°C with the experiment ending at the
606 indicated time by fixation for 20 min at room temperature with 3.7% formaldehyde in
607 PBS. This was followed with a 10-minute incubation of 5µg/mL of Alexa647-labeled
608 wheat germ agglutinin in PBS to label the outline of the cells.

609

610 Cells were imaged using a spinning disk confocal microscope with optical planes
611 spaced 0.3 µm apart (Cocucci et al., 2012). The entry assay scored the presence of
612 MeGFP at the nuclear margin in each cell. Trafficking of viruses to endosomal
613 compartments was observed using live-cell imaging using the spinning disc confocal
614 microscope. Time series with images taken every three seconds for two minutes in a
615 single optical plane with the appropriate fluorescent channels (Cocucci et al., 2012)
616 were acquired from non-fixed samples imaged at the end of the experimental period.
617 For experiments containing NPC1-Halo, the Halo-tagged cells were labeled with either
618 250 nM JF549 or JF647 dye in media for 30 minutes at 37°C. Following labeling, cells
619 were washed three times with media. The microscope was operated using the
620 Slidebook 6.4 software package (3i) and images were displayed also using this
621 software.

622

623 **Statistical tests**

624 To compare the means from cells with different treatments, one-way ANOVA and the
625 *post-hoc* Tukey test analysis were used to take into account unequal sample sizes as
626 indicated in figure legends.

627

628 **ACKNOWLEDGEMENTS**

629 We thank Walter J. Atwood for providing the parental SVG-A cells, Eric Marino, Justin
630 H. Houser and Tegye John Vadakkan for maintaining the spinning disc confocal
631 microscope (T.K. Lab), Marina Cella and Erica Lantelme from the flow cytometry facility,
632 Department of Pathology and Immunology, WUSM for help with flow cytometry,
633 Stephen C. Harrison for helpful discussions and editorial assistance and Alex J. B.
634 Kreutzberger for editorial help. This research was supported by National Institutes of
635 Health funding (AI109740) to S.P.W. and T.K., by MIRA NIH award (GM130386) to T.K.,
636 by National Institutes of Health funding (AI059371) and unrestricted funds from WUSM
637 to S.P.W. and by (75N93019C00062 and R01 AI127828) to M.S.D.

638

639 **AUTHOR CONTRIBUTIONS (NAMES GIVEN AS INITIALS)**

640 T.K., S.P.W., and M.S.D. were responsible for the overall design of the study; Y.K.
641 carried out virus infection, entry and imaging experiments and prepared figures in the
642 lab of T.K. (Fig. 1-5). P.W.R. designed, generated and characterized VSV-eGFP-
643 SARS-CoV-2 and P.Z.L. carried out VSV-chimera infection experiments in the lab of
644 S.P.W. (Fig. 6). J.B.C. and R.E.C. carried out the experiments with authentic SARS-
645 CoV-2 under BSL3 conditions in the lab of M.S.D. (Fig. 7). Recombinant viruses were
646 generated and characterized by D.K.C., S.P., M.R and T.S. in the lab of S.P.W; T.K.
647 drafted the manuscript and editorially reviewed it in close association with SP.W. and
648 M.S.D; the authors commented on the manuscript.

649

650 **COMPETING FINANCIAL INTEREST STATEMENT**

651 M.S.D. is a consultant for Inbios, Vir Biotechnology, NGM Biopharmaceuticals, and on
652 the Scientific Advisory Board of Moderna. The Diamond laboratory at Washington
653 University School of Medicine has received sponsored research agreements from
654 Moderna and Emergent BioSolutions.

655 **REFERENCES**

- 656 Bago, R., Malik, N., Munson, M.J., Prescott, A.R., Davies, P., Sommer, E., Shpiro, N.,
657 Ward, R., Cross, D., Ganley, I.G., et al. (2014). Characterization of VPS34-IN1, a
658 selective inhibitor of Vps34, reveals that the phosphatidylinositol 3-phosphate-binding
659 SGK3 protein kinase is a downstream target of class III phosphoinositide 3-kinase.
660 *Biochem J* 463, 413–427.
- 661 Baranov, M.V., Bianchi, F., Schirmacher, A., van Aart, M.A.C., Maassen, S.,
662 Muntjewerff, E.M., Dingjan, I., Beest, Ter, M., Verdoes, M., Keyser, S.G.L., et al. (2019).
663 The Phosphoinositide Kinase PIKfyve Promotes Cathepsin-S-Mediated Major
664 Histocompatibility Complex Class II Antigen Presentation. *iScience* 11, 160–177.
- 665 Burakoff, R., Barish, C.F., Riff, D., Pruitt, R., Chey, W.Y., Farraye, F.A., Shafran, I.,
666 Katz, S., Krone, C.L., Vander Vliet, M., et al. (2006). A phase 1/2A trial of STA 5326, an
667 oral interleukin-12/23 inhibitor, in patients with active moderate to severe Crohn's
668 disease. *Inflamm Bowel Dis* 12, 558–565.
- 669 Cai, X., Xu, Y., Cheung, A.K., Tomlinson, R.C., Alcázar-Román, A., Murphy, L., Billich,
670 A., Zhang, B., Feng, Y., Klumpp, M., et al. (2013). PIKfyve, a class III PI kinase, is the
671 target of the small molecular IL-12/IL-23 inhibitor apilimod and a player in Toll-like
672 receptor signaling. *Chem Biol* 20, 912–921.
- 673 Cao, W., Henry, M.D., Borrow, P., Yamada, H., Elder, J.H., Ravkov, E.V., Nichol, S.T.,
674 Compans, R.W., Campbell, K.P., and Oldstone, M.B. (1998). Identification of alpha-
675 dystroglycan as a receptor for lymphocytic choriomeningitis virus and Lassa fever virus.
676 *Science* 282, 2079–2081.
- 677 Carette, J.E., Raaben, M., Wong, A.C., Herbert, A.S., Obernosterer, G., Mulherkar, N.,
678 Kuehne, A.I., Kranzusch, P.J., Griffin, A.M., Ruthel, G., et al. (2011). Ebola virus entry
679 requires the cholesterol transporter Niemann-Pick C1. *Nature* 477, 340–343.
- 680 Carlton, J.G., and Cullen, P.J. (2005). Coincidence detection in phosphoinositide
681 signaling. *Trends Cell Biol* 15, 540–547.
- 682 Cerny, J., Feng, Y., Yu, A., Miyake, K., Borgonovo, B., Klumperman, J., Meldolesi, J.,
683 McNeil, P.L., and Kirchhausen, T. (2004). The small chemical vacuolin-1 inhibits
684 Ca²⁺-dependent lysosomal exocytosis but not cell resealing. *EMBO Rep* 5, 883–888.

- 685 Chandran, K., Sullivan, N.J., Felbor, U., Whelan, S.P., and Cunningham, J.M. (2005).
686 Endosomal proteolysis of the Ebola virus glycoprotein is necessary for infection. *308*,
687 1643–1645.
- 688 Chen, C., Lu, Y., Siu, H.M., Guan, J., Zhu, L., Zhang, S., Yue, J., and Zhang, L. (2017).
689 Identification of Novel Vacuolin-1 Analogues as Autophagy Inhibitors by Virtual Drug
690 Screening and Chemical Synthesis. *Molecules* *22*, 891.
- 691 Chou, Y.-Y., Cuevas, C., Carocci, M., Stubbs, S.H., Ma, M., Cureton, D.K., Chao, L.,
692 Evesson, F., He, K., Yang, P.L., et al. (2016). Identification and characterization of a
693 novel broad spectrum virus entry inhibitor. *90*, 4494–4510.
- 694 Cocucci, E., Aguet, F., Boulant, S., and Kirchhausen, T. (2012). The first five seconds in
695 the life of a clathrin-coated pit. *150*, 495–507.
- 696 Côté, M., Misasi, J., Ren, T., Bruchez, A., Lee, K., Filone, C.M., Hensley, L., Li, Q., Ory,
697 D., Chandran, K., et al. (2011). Small molecule inhibitors reveal Niemann-Pick C1 is
698 essential for Ebola virus infection. *Nature* *477*, 344–348.
- 699 Dyall, J., Nelson, E.A., DeWald, L.E., Guha, R., Hart, B.J., Zhou, H., Postnikova, E.,
700 Logue, J., Vargas, W.M., Gross, R., et al. (2018). Identification of Combinations of
701 Approved Drugs With Synergistic Activity Against Ebola Virus in Cell Cultures. *J. Infect.*
702 *Dis.* *218*, S672–S678.
- 703 Glowacka, I., Bertram, S., Müller, M.A., Allen, P., Soilleux, E., Pfefferle, S., Steffen, I.,
704 Tsegaye, T.S., He, Y., Gnirss, K., et al. (2011). Evidence that TMPRSS2 activates the
705 severe acute respiratory syndrome coronavirus spike protein for membrane fusion and
706 reduces viral control by the humoral immune response. *J. Virol.* *85*, 4122–4134.
- 707 Hoffmann, M., Kleine-Weber, H., Schroeder, S., Krüger, N., Herrler, T., Erichsen, S.,
708 Schiergens, T.S., Herrler, G., Wu, N.-H., Nitsche, A., et al. (2020). SARS-CoV-2 Cell
709 Entry Depends on ACE2 and TMPRSS2 and Is Blocked by a Clinically Proven Protease
710 Inhibitor. *Cell* *181*, 271–280.e278.
- 711 Hulseberg, C.E., Fénéant, L., Szymańska-de Wijs, K.M., Kessler, N.P., Nelson, E.A.,
712 Shoemaker, C.J., Schmaljohn, C.S., Polyak, S.J., and White, J.M. (2019). Arbidol and
713 Other Low-Molecular-Weight Drugs That Inhibit Lassa and Ebola Viruses. *J. Virol.* *93*,
714 11.

- 715 Ikonomov, O.C., Sbrissa, D., and Shisheva, A. (2001). Mammalian cell morphology and
716 endocytic membrane homeostasis require enzymatically active phosphoinositide 5-
717 kinase PIKfyve. *J Biol Chem* 276, 26141–26147.
- 718 Ikonomov, O.C., Sbrissa, D., Delvecchio, K., Xie, Y., Jin, J.-P., Rappolee, D., and
719 Shisheva, A. (2011). The phosphoinositide kinase PIKfyve is vital in early embryonic
720 development: preimplantation lethality of PIKfyve^{-/-} embryos but normality of PIKfyve^{+/-}
721 mice. *Journal of Biological Chemistry* 286, 13404–13413.
- 722 Ikonomov, O.C., Sbrissa, D., Mlak, K., Kanzaki, M., Pessin, J., and Shisheva, A. (2002).
723 Functional dissection of lipid and protein kinase signals of PIKfyve reveals the role of
724 PtdIns 3,5-P₂ production for endomembrane integrity. *J Biol Chem* 277, 9206–9211.
- 725 Ikonomov, O.C., Sbrissa, D., Mlak, K., Deeb, R., Fligger, J., Soans, A., Finley, R.L., and
726 Shisheva, A. (2003). Active PIKfyve associates with and promotes the membrane
727 attachment of the late endosome-to-trans-Golgi network transport factor Rab9 effector
728 p40. *J Biol Chem* 278, 50863–50871.
- 729 Jae, L.T., Raaben, M., Herbert, A.S., Kuehne, A.I., Wirchnianski, A.S., Soh, T.K.,
730 Stubbs, S.H., Janssen, H., Damme, M., Saftig, P., et al. (2014). Virus entry. Lassa virus
731 entry requires a trigger-induced receptor switch. *Science* 344, 1506–1510.
- 732 Jefferies, H.B.J., Cooke, F.T., Jat, P., Boucheron, C., Koizumi, T., Hayakawa, M.,
733 Kaizawa, H., Ohishi, T., Workman, P., Waterfield, M.D., et al. (2008). A selective
734 PIKfyve inhibitor blocks PtdIns(3,5)P₂ production and disrupts endomembrane
735 transport and retroviral budding. *EMBO Rep* 9, 164–170.
- 736 Krausz, S., Boumans, M.J.H., Gerlag, D.M., Lufkin, J., van Kuijk, A.W.R., Bakker, A., de
737 Boer, M., Lodde, B.M., Reedquist, K.A., Jacobson, E.W., et al. (2012). Brief report: a
738 phase IIa, randomized, double-blind, placebo-controlled trial of apilimod mesylate, an
739 interleukin-12/interleukin-23 inhibitor, in patients with rheumatoid arthritis. *Arthritis*
740 *Rheum.* 64, 1750–1755.
- 741 Le Blanc, I., Luyet, P.-P., Pons, V., Ferguson, C., Emans, N., Petiot, A., Mayran, N.,
742 Demareux, N., Fauré, J., Sadoul, R., et al. (2005). Endosome-to-cytosol transport of
743 viral nucleocapsids. *Nat Cell Biol* 7, 653–664.
- 744 Lu, Y., Dong, S., Hao, B., Li, C., Zhu, K., Guo, W., Wang, Q., Cheung, K.-H., Wong,

- 745 C.W., Wu, W.-T., et al. (2014). Vacuolin-1 potently and reversibly inhibits
746 autophagosome-lysosome fusion by activating RAB5A. *Autophagy* 10, 1895–1905.
- 747 Matsuyama, S., Nagata, N., Shirato, K., Kawase, M., Takeda, M., and Taguchi, F.
748 (2010). Efficient activation of the severe acute respiratory syndrome coronavirus spike
749 protein by the transmembrane protease TMPRSS2. *J. Virol.* 84, 12658–12664.
- 750 Nelson, C.D.S., Derdowski, A., Maginnis, M.S., O'Hara, B.A., and Atwood, W.J. (2012).
751 The VP1 subunit of JC polyomavirus recapitulates early events in viral trafficking and is
752 a novel tool to study polyomavirus entry. *Virology* 428, 30–40.
- 753 Nelson, E.A., Dyllal, J., Hoenen, T., Barnes, A.B., Zhou, H., Liang, J.Y., Michelotti, J.,
754 Dewey, W.H., DeWald, L.E., Bennett, R.S., et al. (2017). The phosphatidylinositol-3-
755 phosphate 5-kinase inhibitor apilimod blocks filoviral entry and infection. *PLoS Negl*
756 *Trop Dis* 11, e0005540.
- 757 Ou, X., Liu, Y., Lei, X., Li, P., Mi, D., Ren, L., Guo, L., Guo, R., Chen, T., Hu, J., et al.
758 (2020). Characterization of spike glycoprotein of SARS-CoV-2 on virus entry and its
759 immune cross-reactivity with SARS-CoV. *Nat Commun* 11, 1–12.
- 760 Pasqual, G., Rojek, J.M., Masin, M., Chatton, J.-Y., and Kunz, S. (2011). Old world
761 arenaviruses enter the host cell via the multivesicular body and depend on the
762 endosomal sorting complex required for transport. *PLoS Pathog* 7, e1002232.
- 763 Qiu, S., Leung, A., Bo, Y., Kozak, R.A., Anand, S.P., Warkentin, C., Salambanga,
764 F.D.R., Cui, J., Kobinger, G., Kobasa, D., et al. (2018). Ebola virus requires
765 phosphatidylinositol (3,5) bisphosphate production for efficient viral entry. *Virology* 513,
766 17–28.
- 767 Ran, F.A., Hsu, P.D., Wright, J., Agarwala, V., Scott, D.A., and Zhang, F. (2013).
768 Genome engineering using the CRISPR-Cas9 system. *Nat Protoc* 8, 2281–2308.
- 769 Rutherford, A.C., Traer, C., Wassmer, T., Pattni, K., Bujny, M.V., Carlton, J.G.,
770 Stenmark, H., and Cullen, P.J. (2006). The mammalian phosphatidylinositol 3-
771 phosphate 5-kinase (PIKfyve) regulates endosome-to-TGN retrograde transport. *J Cell*
772 *Sci* 119, 3944–3957.
- 773 Sands, B.E., Jacobson, E.W., Sylwestrowicz, T., Younes, Z., Dryden, G., Fedorak, R.,
774 and Greenbloom, S. (2010). Randomized, double-blind, placebo-controlled trial of the

- 775 oral interleukin-12/23 inhibitor apilimod mesylate for treatment of active Crohn's
776 disease. *Inflamm Bowel Dis* *16*, 1209–1218.
- 777 Sano, O., Kazetani, K., Funata, M., Fukuda, Y., Matsui, J., and Iwata, H. (2016).
778 Vacuolin-1 inhibits autophagy by impairing lysosomal maturation via PIKfyve inhibition.
779 *FEBS Lett* *590*, 1576–1585.
- 780 Sbrissa, D., Ikononov, O.C., and Shisheva, A. (1999). PIKfyve, a mammalian ortholog
781 of yeast Fab1p lipid kinase, synthesizes 5-phosphoinositides. Effect of insulin. *J Biol*
782 *Chem* *274*, 21589–21597.
- 783 Sbrissa, D., Ikononov, O.C., Fu, Z., Ijuin, T., Gruenberg, J., Takenawa, T., and
784 Shisheva, A. (2007). Core protein machinery for mammalian phosphatidylinositol 3,5-
785 bisphosphate synthesis and turnover that regulates the progression of endosomal
786 transport. Novel Sac phosphatase joins the ArPIKfyve-PIKfyve complex. *J Biol Chem*
787 *282*, 23878–23891.
- 788 Schornberg, K., Matsuyama, S., Kabsch, K., Delos, S., Bouton, A., and White, J. (2006).
789 Role of endosomal cathepsins in entry mediated by the Ebola virus glycoprotein. *80*,
790 4174–4178.
- 791 Sharma, G., Guardia, C.M., Roy, A., Vassilev, A., Saric, A., Griner, L.N., Marugan, J.,
792 Ferrer, M., Bonifacino, J.S., and DePamphilis, M.L. (2019). A family of PIKFYVE
793 inhibitors with therapeutic potential against autophagy-dependent cancer cells disrupt
794 multiple events in lysosome homeostasis. *Autophagy* *15*, 1694–1718.
- 795 Shisheva, A., Sbrissa, D., and Ikononov, O. (1999). Cloning, characterization, and
796 expression of a novel Zn²⁺-binding FYVE finger-containing phosphoinositide kinase in
797 insulin-sensitive cells. *Mol Cell Biol* *19*, 623–634.
- 798 Shulla, A., Heald-Sargent, T., Subramanya, G., Zhao, J., Perlman, S., and Gallagher, T.
799 (2011). A transmembrane serine protease is linked to the severe acute respiratory
800 syndrome coronavirus receptor and activates virus entry. *J. Virol.* *85*, 873–882.
- 801 Simmons, G., Gosalia, D.N., Rennekamp, A.J., Reeves, J.D., Diamond, S.L., and
802 Bates, P. (2005). Inhibitors of cathepsin L prevent severe acute respiratory syndrome
803 coronavirus entry. *Proc Natl Acad Sci USA* *102*, 11876–11881.
- 804 Simmons, G., Reeves, J.D., Rennekamp, A.J., Amberg, S.M., Piefer, A.J., and Bates, P.

- 805 (2004). Characterization of severe acute respiratory syndrome-associated coronavirus
806 (SARS-CoV) spike glycoprotein-mediated viral entry. *Proc Natl Acad Sci USA* *101*,
807 4240–4245.
- 808 Soh, T.K., and Whelan, S.P.J. (2015). Tracking the Fate of Genetically Distinct
809 Vesicular Stomatitis Virus Matrix Proteins Highlights the Role for Late Domains in
810 Assembly. *89*, 11750–11760.
- 811 Spence, J.S., Krause, T.B., Mittler, E., Jangra, R.K., and Chandran, K. (2016). Direct
812 Visualization of Ebola Virus Fusion Triggering in the Endocytic Pathway. *MBio* *7*,
813 e01857–15.
- 814 Wada, Y., Cardinale, I., Khatcherian, A., Chu, J., Kantor, A.B., Gottlieb, A.B., Tatsuta,
815 N., Jacobson, E., Barsoum, J., and Krueger, J.G. (2012). Apilimod inhibits the
816 production of IL-12 and IL-23 and reduces dendritic cell infiltration in psoriasis. *PLoS*
817 *ONE* *7*, e35069.
- 818 Wang, H., Yang, P., Liu, K., Guo, F., Zhang, Y., Zhang, G., and Jiang, C. (2008). SARS
819 coronavirus entry into host cells through a novel clathrin- and caveolae-independent
820 endocytic pathway. *Cell Res* *18*, 290–301.
- 821 Whelan, S.P., Ball, L.A., Barr, J.N., and Wertz, G.T. (1995). Efficient recovery of
822 infectious vesicular stomatitis virus entirely from cDNA clones. *Proc Natl Acad Sci USA*
823 *92*, 8388–8392.
- 824 Wong, A.C., Sandesara, R.G., Mulherkar, N., Whelan, S.P., and Chandran, K. (2010). A
825 forward genetic strategy reveals destabilizing mutations in the Ebolavirus glycoprotein
826 that alter its protease dependence during cell entry. *J. Virol.* *84*, 163–175.
- 827 Yuan, M., Wu, N.C., Zhu, X., Lee, C.-C.D., So, R.T.Y., Lv, H., Mok, C.K.P., and Wilson,
828 I.A. (2020). A highly conserved cryptic epitope in the receptor-binding domains of
829 SARS-CoV-2 and SARS-CoV. *Science* eabb7269.

830

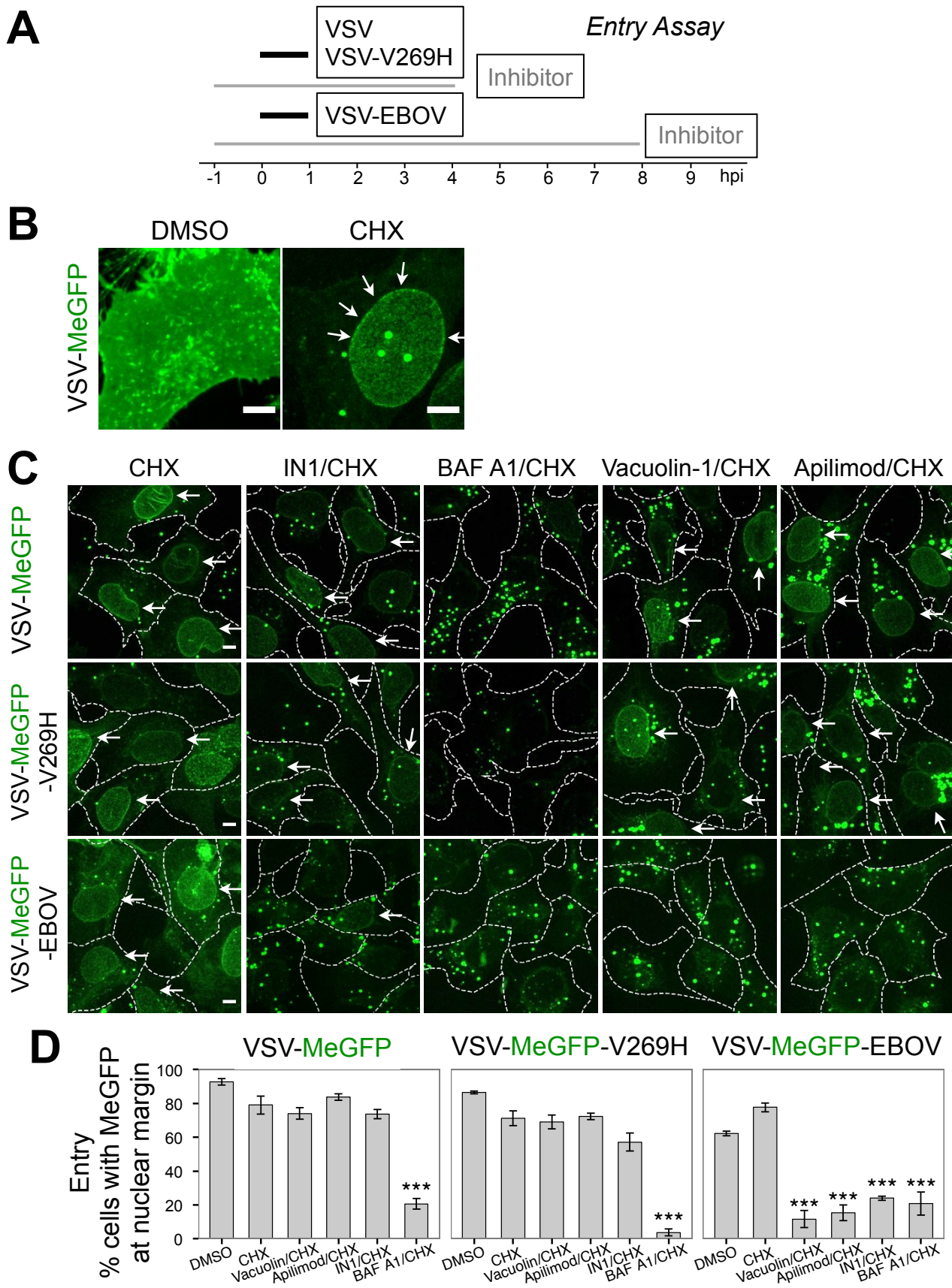
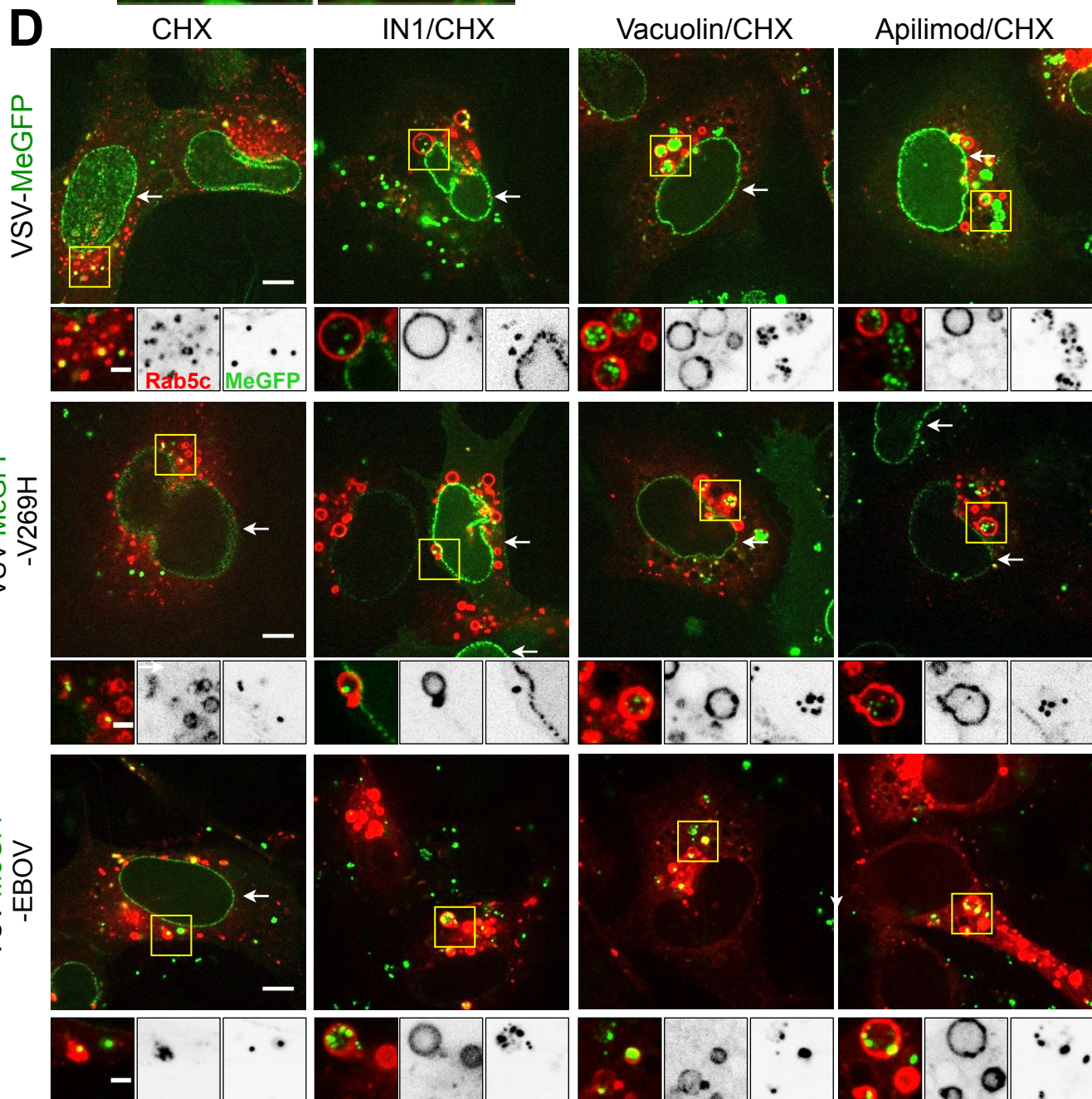
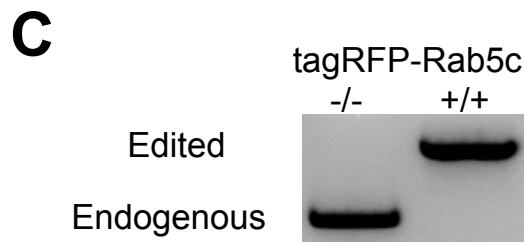
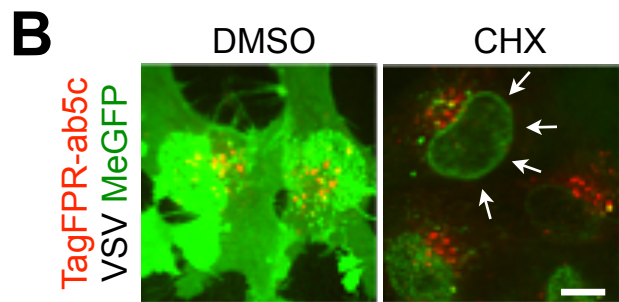
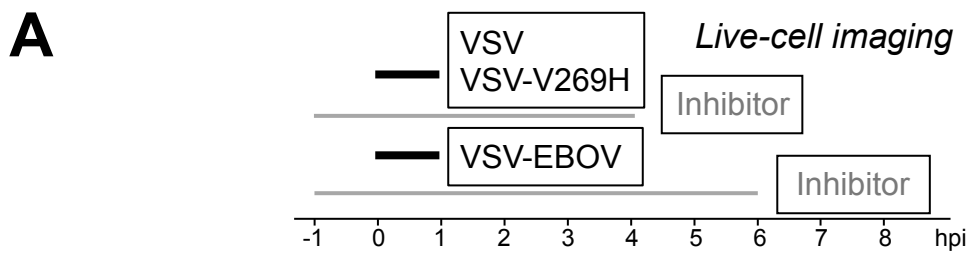


Figure 2



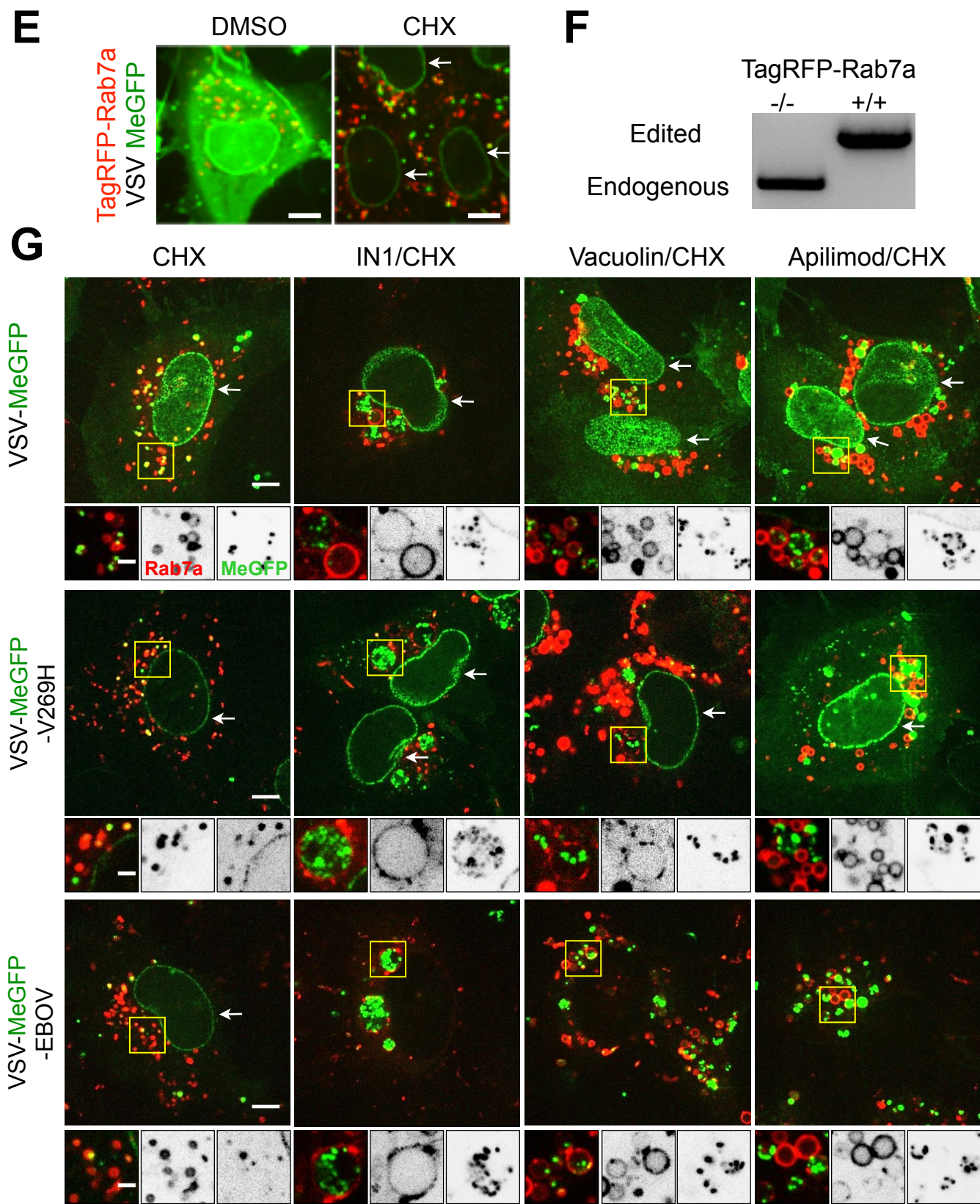


Figure 3

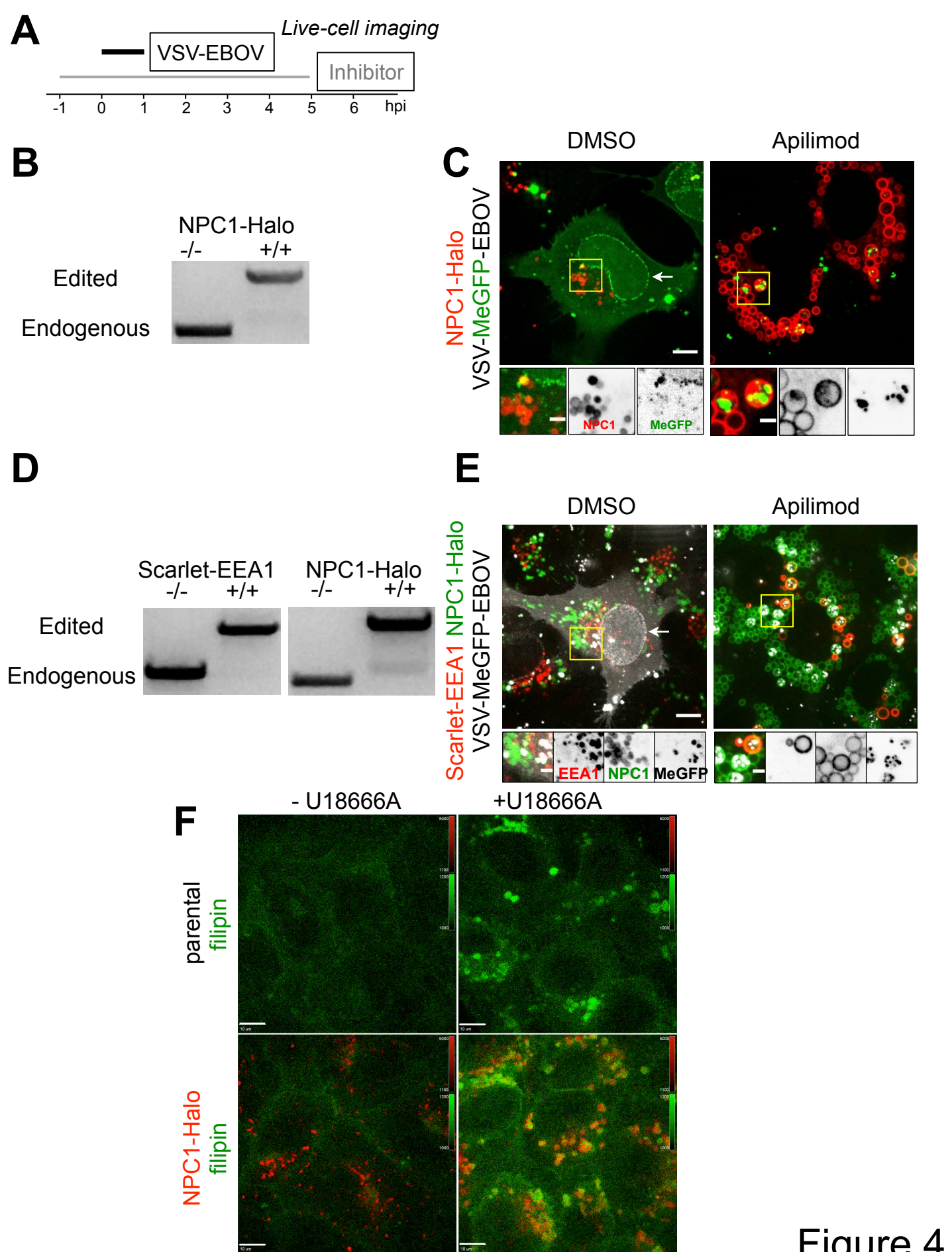


Figure 4

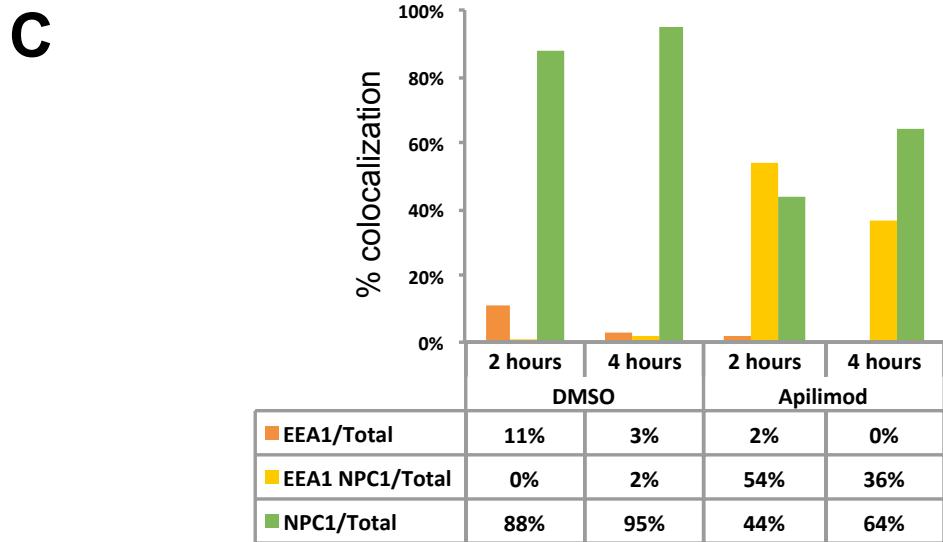
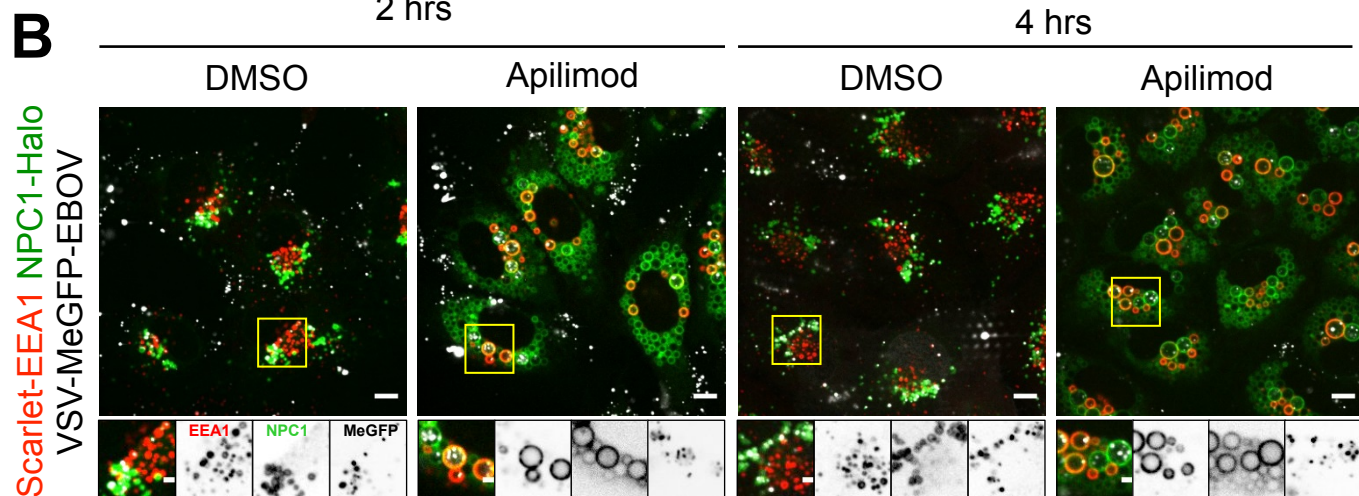
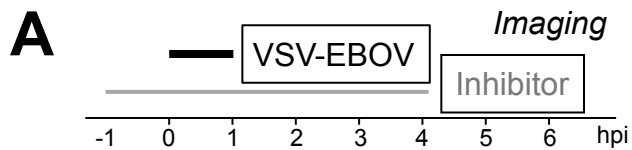


Figure 5

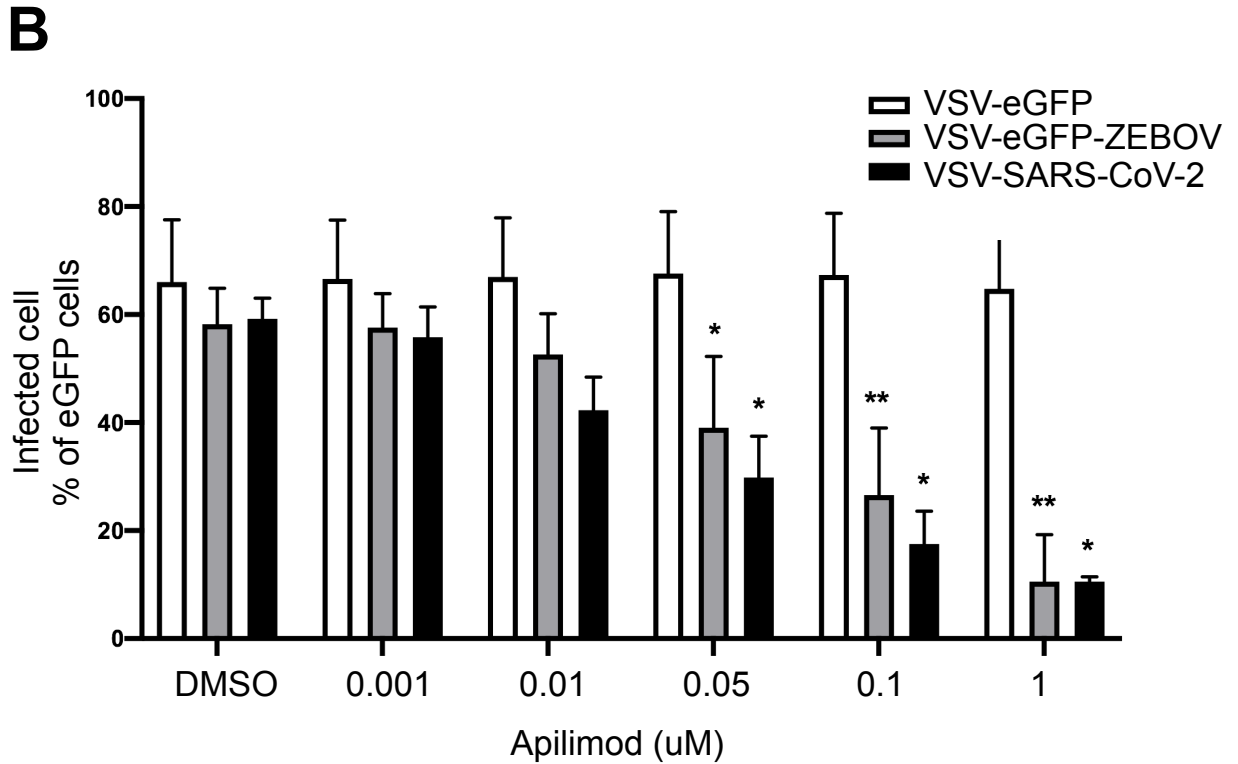
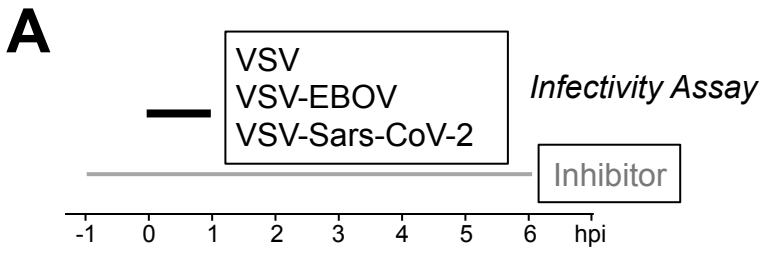


Figure 6

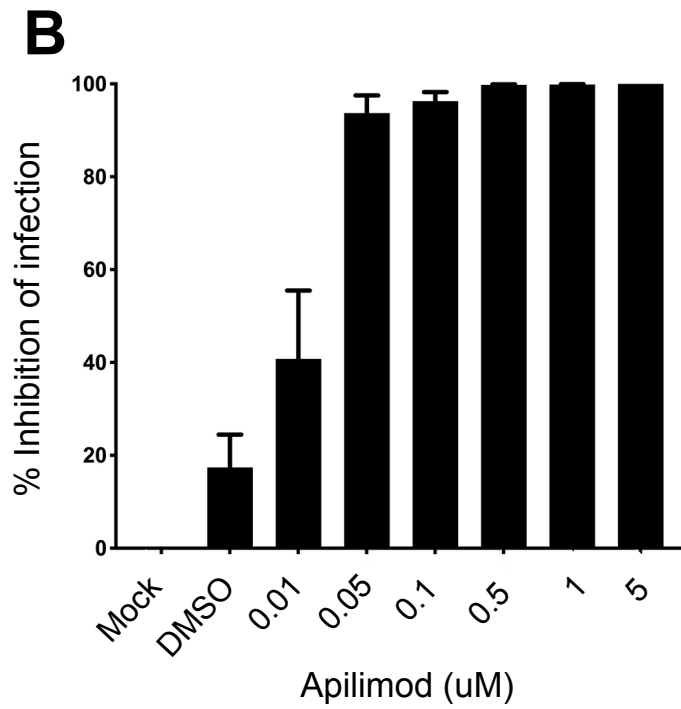
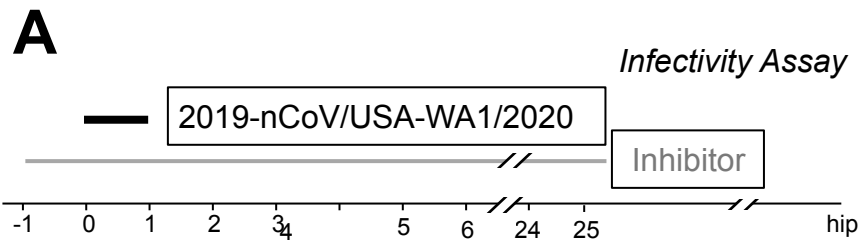


Figure 7